Equatorial scintillation calculations based on coherent scatter radar and C/NOFS data

Emanoel Costa,[1] Eurico R. de Paula,[2] L. F. C. Rezende,[2] Keith M. Groves,[3] Patrick A. Roddy,[3] Eugene V. Dao,[4] and Michael C. Kelley[4]

Received 21 May 2010; revised 3 December 2010; accepted 20 January 2011; published 7 April 2011.

[1] During its transit through a region of equatorial ionospheric irregularities, sensors on board the Communication/Navigation Outage Forecasting System (C/NOFS) satellite provide a one-dimensional description of the medium, which can be extended to two dimensions if the structures are assumed to be elongated in the direction of the magnetic field lines. The C/NOFS scintillation calculation approach assumes that the medium is equivalent to a diffracting screen with random phase fluctuations that are proportional to the irregularities in the total electron content, specified through the product of the directly measured electron density by an estimated extent of the irregularity layer along the raypaths. Within the international collaborative effort anticipated by the C/NOFS Science Definition Team, the present work takes the vertical structure of the irregularities into more detailed consideration, which could lead to improved predictions of scintillation. Initially, it describes a flexible model for the power spectral density of the equatorial ionospheric irregularities, estimates its shape parameters from C/NOFS in situ data and uses the signal-to-noise ratio S/N measurements by the São Luís coherent scatter radar to estimate the mean square electron density fluctuation $\langle \Delta N^2 \rangle$ within the corresponding sampled volume. Next, it presents an algorithm for the wave propagation through a three-dimensional irregularity layer which considers the variations of $\langle \Delta N^2 \rangle$ along the propagation paths according to observations by the radar. Data corresponding to several range-time-intensity maps from the radar is used to predict time variations of the scintillation index S_4 at the L1 Global Positioning System (GPS) frequency (1575.42 MHz). The results from the scintillation calculations are compared with corresponding measurements by the colocated São Luís GPS scintillation monitor for an assessment of the prediction capability of the present formulation.

Citation: Costa, E., E. R. de Paula, L. F. C. Rezende, K. M. Groves, P. A. Roddy, E. V. Dao, and M. C. Kelley (2011), Equatorial scintillation calculations based on coherent scatter radar and C/NOFS data, *Radio Sci.*, *46*, RS2011, doi:10.1029/2010RS004435.

1. Introduction

[2] Ionospheric scintillation exhibits extreme variability in space and time, significantly degrading both the performance and the availability of space-based communication and navigation systems. For example, amplitude fading increases the transmission bit error rate (BER) in both systems and, in particular, causes data loss and cycle slips in Global Positioning System (GPS) receivers. Severe phase scintillation may cause these receivers to lose phase lock. The most intense scintillation events may render these systems unavailable for long time intervals [*Groves et al.*, 1997; *Basu et al.*, 2002]. Under such conditions, it is very difficult for the operator of these systems to decide if either equipment failure or propagation impairment occurred, and then which correcting or mitigating action to take. For the support of satellite communication and navigation systems, short-

[1]Centro de Estudos em Telecomunicações, Pontifícia Universidade Católica do Rio de Janeiro, Rio de Janeiro, Brazil.
[2]Divisão de Aeronomia, Instituto Nacional de Pesquisas Espaciais, São José dos Campos, Brazil.
[3]Space Vehicles Directorate, Air Force Research Laboratory, Hanscom Air Force Base, Massachussetts, USA.
[4]School of Electrical and Computer Engineering, Cornell University, Ithaca, New York, USA.

0048-6604/11/2010RS004435

term specification and forecast systems based on real-time measurements are needed.

[3] One such system, the Scintillation Network Decision Aid (SCINDA), has been developed for the equatorial region [*Groves et al.*, 1997; *Caton et al.*, 2004]. It combines measurements from several sites distributed along the equatorial belt (absolute value of geomagnetic latitude less than approximately 20°) by using 250 MHz and L1 (1575.42 MHz) transmissions from geostationary and GPS satellites, respectively. The data drive a scintillation model which also uses upward and zonal motions of irregularities to produce a three-dimensional visualization of scintillation structures which is updated four times per hour and communication outage maps for selected satellites. As a result, SCINDA is able to provide short-term forecasts of scintillation to users located east of the observing stations.

[4] The Communication/Navigation Outage Forecasting System (C/NOFS) is an orbiting satellite with an inclination of 13°, a perigee of 400 km and an apogee of 850 km, launched on 16 April 2008. Data from sensors on board the satellite drive an equatorial ionospheric model to forecast the onset of plasma instability, as well as its evolution into plasma bubbles [*Retterer*, 2010]. Due to its orbital period, the satellite is able to track these processes at 90 min intervals. The list of C/NOFS science objectives has been organized into three categories: (1) to understand physical processes active in the background ionosphere and thermosphere in which plasma instabilities grow; (2) to identify mechanisms that trigger or quench the plasma irregularities; and (3) to determine how the plasma irregularities affect the propagation of electromagnetic waves. It is anticipated that, by the end of the C/NOFS mission, with the assimilation of data from other ground- and space-based instruments and systems (incoherent and coherent radars, SCINDA, DMSP, etc.), the understanding of the physics controlling the equatorial ionosphere will have advanced to the point that the operational objective will also be reached: to nowcast and forecast the formation of ionospheric irregularities and their effects on the propagation of electromagnetic waves to a high degree of accuracy. It should be observed that a 2 h to 6 h forecast is required, as well as an extended 72 h prediction [*de La Beaujardière et al.*, 2004].

[5] Sensors on board any spacecraft transiting through a volume of irregularities along a low-inclination orbit will detect electron density fluctuations. However, the corresponding data only provide a one-dimensional description of the medium, which can be extended to two dimensions if the structures are assumed to be elongated in the direction the magnetic field lines. The C/NOFS Science Definition Team selected a phase screen approach for the estimation of scintillation statistics [*de La Beaujardière et al.*, 2004]. This estimation can be validated by scintillation measurements performed using transmissions from the Coherent Electromagnetic Radio Tomography (CERTO) tri-frequency (150 MHz, 400 MHz and 1067 MHz) beacon. The phase-screen approach [*Yeh and Liu*, 1982; *Knepp*, 1983; *Rino and Owen*, 1984; *Beach et al.*, 2004] assumes that the medium is equivalent to a diffracting screen with random phase fluctuations that are proportional to the irregularities in the total electron content (TEC), specified through the product of the directly measured electron density by an estimated extent of the irregularity layer along the raypaths between orbital and terrestrial transceivers. It is also reasonable to assume that the irregularities are frozen to the medium and drift across the field lines in the magnetic east-west direction, particularly for those field lines sampled appropriately after the local sunset, when the generation processes and the nonlinear evolution into upwelling bubbles are no longer present. As the wave propagates in free space below the screen, phase and amplitude fluctuations begin to develop. This approach was used to derive different moments of the amplitude and the phase of the received signal by many authors [*Yeh and Liu*, 1982, and references therein]. These analytical studies were performed in both the thin-screen (small RMS phase fluctuation) and the thick-screen (large RMS phase fluctuation) regimes, assuming appropriate statistics for the phase fluctuations of the emerging wavefront. An alternative to these studies has been the representation of the irregular ionosphere by multiple screens to numerically characterize the signals received on the ground. This method, which can also be used when scattering is relatively strong, repeatedly uses the known field at a certain screen to determine the field at the next one [*Knepp*, 1983; *Rino and Owen*, 1984].

[6] In spite of the success of the above approach, it is necessary to investigate whether more detailed consideration of the vertical structure of the irregularities could lead to improved predictions of scintillation. Information on the vertical structure of irregularities would be provided in the ideal format by rocket in situ measurements during experimental campaigns coordinated with the transits of the C/NOFS satellite over the launch sites, possibly with the support of coherent scatter radars such as the ones located at the Jicamarca (11.95°S, 76.87°W, dip angle 1.32°, magnetic latitude 1.46°S), São Luís (2.57°S, 44.21°W, dip angle −2.70°, magnetic latitude 6.73°N) and Kwajalein (8.8°N, 167.5°E, dip angle 7.90°, magnetic latitude 3.25°N) Observatories. Although ideal, this data would unfortunately also be scarcely available in time and space, and description of the vertical structure of the irregularities for forecasting of ionospheric scintillation cannot depend entirely on it. With the necessary regularity (that is, for all near-overhead passes of the C/NOFS satellite), this information can only be provided by radars, which probe irregularities with scale sizes much smaller than the ones causing scintillation, with

spatial resolutions significantly worse than that from in situ measurements. In principle, a relatively coarse spatial resolution may seem inappropriate for the present application. However, the results from experimental campaigns [*Kelley et al.*, 1986; *LaBelle et al.*, 1997] showed a good correlation between the occurrence of depletions and structures with sharp gradients in rocket data and the strength of backscatter power from the corresponding plumes of irregularities simultaneously observed by the radar. The present effort may also be facilitated by the recent demonstration [*Beach et al.*, 2004] that the scintillation index S_4 (a parameter which characterizes the strength of scintillation, defined by the standard deviation of $I/ < I >$, where I is the random variable which represents the intensity fluctuations of the received signal and $< I >$ is its mean value) can be estimated with acceptable errors using sparsely sampled data.

[7] The present work is being performed within the international collaborative effort anticipated by the C/NOFS Science Definition Team. Its objectives are to develop the above concepts in detail and to apply them more extensively, analyzing their effectiveness and limitations. More specifically, section 2 will describe a flexible model for the power spectral density of the equatorial ionospheric irregularities, estimate its shape parameters from C/NOFS in situ data and use the signal-to-noise ratio S/N measurements by coherent scatter radars to estimate the mean square electron density fluctuation $\langle \Delta N^2 \rangle$ within the corresponding sampled volume. Assumptions leading to this relationship, as well as its restrictions, will be discussed, with the support of Appendix A. Next, section 3 will briefly describe a discrete algorithm for the wave propagation through a three-dimensional irregularity layer, developed in detail in Appendix B. The algorithm solves a parabolic approximation [*Wernik et al.*, 1980] to the wave equation, valid when partial reflections are negligible, by subdividing the layer into multiple statistically homogeneous thin slabs, followed by the repeated application of the Huygens-Fresnel diffraction theory [*Goodman*, 1968] to each of them. This development extends previous work by *Costa and Basu* [2002] to three dimensions and shows how both versions could lead to the single phase-screen model as a special case. The algorithm considers the variations of $\langle \Delta N^2 \rangle$ along the propagation paths as indirectly measured by the coherent scatter radar, according to the prescriptions of section 2. In section 4, data corresponding to several range-time-intensity (RTI) maps from the São Luís coherent scatter radar, which is part of the Instituto Nacional de Pesquisas Espaciais (INPE) Observatory, will be used to predict time variations of the scintillation index S_4 at the L1 GPS frequency. The results will be compared with corresponding measurements by the colocated São Luís GPS scintillation monitor to assess the prediction capability of the present formulation. Together with the conclusions, section 5 will also consider how the present scintillation calculations could be improved by more extensive use of ground and C/NOFS in situ data.

2. Power Spectral Density Model of the Irregularities: Estimation of Parameters From Coherent Scatter Radar and in Situ Measurements

[8] The random electron density fluctuations δN in each volume of the irregularity layer will be characterized by the following three-dimensional spectral density model [*Walker et al.*, 1987]

$$S_N^{3D}\left(\vec{k}\right) = S_N^{3D}\left(k_x, k_y, k_z\right) = S_o \langle \Delta N^2 \rangle \exp\left[-a^2 \frac{k_y^2/k_o^2}{1 + k_\perp^2/k_o^2}\right] S_\perp(k_\perp) \qquad (1)$$

In expression (1), (k_x, k_y, k_z) are the components of the wave vector in west-east, magnetic field, and upward directions, respectively, $\langle \Delta N^2 \rangle$ is the mean square electron fluctuation, $k_o = 2\pi/L_o$, L_o is the outer scale size, $k_\perp^2 = k_x^2 + k_z^2$, and a is a dimensionless anisotropy constant. The following expression will be assumed for the function $S_\perp(k_\perp)$

$$S_\perp(k_\perp) = \begin{cases} \left(1 + k_\perp^2/k_o^2\right)^{-\frac{p+1}{2}} & for \quad k_\perp^2 < k_b^2 \\ \left(1 + k_b^2/k_o^2\right)^{-\frac{p}{2}} \left(1 + k_\perp^2/k_o^2\right)^{-\frac{1}{2}} \left(k_\perp^2/k_b^2\right)^{-\frac{q}{2}} & for \quad k_\perp^2 \geq k_b^2 \end{cases} \qquad (2)$$

Expression (2) characterizes a spectral break at $k_b = 2\pi/L_b$, where L_b is the breakpoint scale size, as well as the spectral indices p and q for $k_\perp^2 < k_b^2$ and $k_\perp^2 > k_b^2$, respectively. The above representation is flexible enough to provide good agreement with one-dimensional power spectral densities resulting from in situ measurements of electron density fluctuations across the geomagnetic field. However, as remarked by *Walker et al.* [1987], the

dependence of the power spectral density along the magnetic field is not well known and may play a role in the calculations to be described. One interesting feature of the Gaussian behavior with an additional dependence on $k_\perp$, proposed by these authors, is that the elongation of the irregularities varies with their perpendicular width in a statistical sense.

[9] It is well known that the three-dimensional correlation function $\langle \Delta N^2 \rangle \ \rho_N^{3D}(\vec{r})$ is the inverse Fourier Transform of $S_N^{3D}(\vec{k})$. Combining this relationship with the usual normalization $\rho_N^{3D}(\vec{0}) = 1$, it follows that the constant S_o in expression (1) should satisfy the condition

$$\int_{-\infty}^{+\infty}\int\int S_N^{3D}\left(\vec{k}\right) dk_x dk_y dk_z = (2\pi)^3 \langle \Delta N^2 \rangle \qquad (3)$$

Substituting expressions (1) and (2) into the integrand of equation (3), one gets

$$(S_o/a) = \frac{8\pi\sqrt{\pi}}{k_o^3}\left\{\frac{1}{\left(\frac{p}{2}-1\right)}\left[1-\frac{1}{\left(1+k_b^2/k_o^2\right)^{\frac{p}{2}-1}}\right] + \frac{1}{\left(\frac{q}{2}-1\right)}\cdot\frac{\left(k_b^2/k_o^2\right)}{\left(1+k_b^2/k_o^2\right)^{\frac{p}{2}}}\right\}^{-1} = \frac{8\pi\sqrt{\pi}}{k_o^3 S_1} \qquad (4)$$

The two- and one-dimensional spectral densities of the random electron fluctuations δN are obtained from successive integrations of expression (1), in combination with expression (2), as follows

$$S_N^{2D}(k_x,k_z) = \frac{1}{2\pi}\int_{-\infty}^{+\infty} S_N^{3D}\left(\vec{k}\right) dk_y = \frac{4\pi}{k_o^2 S_1}\langle \Delta N^2 \rangle \cdot \cdot \begin{cases} \left(1+k_\perp^2/k_o^2\right)^{-\frac{p}{2}} & for \quad k_\perp^2 < k_b^2 \\ \left(1+k_b^2/k_o^2\right)^{-\frac{p}{2}}\left(k_\perp^2/k_b^2\right)^{-\frac{q}{2}} & for \quad k_\perp^2 \geq k_b^2 \end{cases} \qquad (5)$$

and

where $r_1 = \sqrt{\left(k_b^2-k_x^2\right)/\left(k_o^2+k_x^2\right)}$, $r_2 = \sqrt{\left(k_b^2-k_x^2\right)/k_x^2}$, and

$$F(u,v) = \int_0^u \frac{dt}{\left(1+t^2\right)^{v/2}} \qquad (7)$$

It should be observed that expressions (5) and (6) are continuous at $k_\perp^2 = k_x^2 + k_z^2 = k_b^2$ and $k_x^2 = k_b^2$, respectively, as desired. The values of the shape parameters L_o, L_b, p, and q of the spectral model can be estimated by matching expression (6) to results from in situ measurements of electron density fluctuations and can be independently specified with total flexibility, at the cost of a more involved expression for the regime $k_x^2 < k_b^2$. These results consistently show that $L_o \gg L_b$ and that $p < q$. Rocket in situ electron density data [*Singh and Szuszczewicz*, 1984; *LaBelle et al.*, 1986; *Hysell et al.*, 1994a, 1994b; *Hysell*, 2000; *Muralikrishna et al.*, 2003] from altitudes above 280 km have shown double-slope one-dimensional power spectral densities with spectral indices (p-1) between 1.9 and 2.5 for medium-scale sizes and (q-1) between 4.5 and 5.0 for small-scale sizes. The typical value for the outer scale size is $L_o \approx 12.5$ km and the scale size of the spectral break point has been found in the vicinity of 60 m to 100 m. However, it should be remembered that in situ satellite measurements [*Basu et al.*, 1983; *Singh and Szuszczewicz*, 1984] yielded smaller values for the spectral indices (p-1) and (q-1), indicating shallower power spectral densities than those indicated above. Fixed values for the spectral shape parameters have been selected for the future calculations by matching the one-dimensional power spectral density model to average results from recent in situ C/NOFS Planar Langmuir Probe (PLP) measurements of electron density fluctuations from 0015 UT to 0030 UT on 12 November 2008 (orbit 3106), from 2347 UT to 2357 UT on 2 December 2008 (orbit 3417), and from 2309 UT to 2320 UT on 4 December 2008 (orbit 3446). During these passes, the elevation of the raypath from the São Luís Observatory to the C/NOFS satellite reached high values and relatively strong irregularities were simultaneously observed. Note

$$S_N^{1D}(k_x) = \frac{1}{2\pi}\int_{-\infty}^{+\infty} S_N^{2D}(k_x,k_z)dk_z = \frac{4\pi}{k_o S_1}\langle \Delta N^2 \rangle \cdot \cdot \begin{cases} \dfrac{F(r_1,p)}{\left(1+k_x^2/k_o^2\right)^{(p-1)/2}} + \dfrac{\left(k_b/k_o\right)}{\left(1+k_b^2/k_o^2\right)^{p/2}}\cdot\dfrac{\frac{\sqrt{\pi}}{2}\cdot\frac{\Gamma\left(\frac{q-1}{2}\right)}{\Gamma\left(\frac{q}{2}\right)} - F(r_2,p)}{\left(k_x^2/k_b^2\right)^{(q-1)/2}} & for \quad k_x^2 < k_b^2 \\ \dfrac{\sqrt{\pi}}{2}\cdot\dfrac{\Gamma\left(\frac{q-1}{2}\right)}{\Gamma\left(\frac{q}{2}\right)}\cdot\dfrac{\left(k_b/k_o\right)}{\left(1+k_b^2/k_o^2\right)^{p/2}}\cdot\dfrac{1}{\left(k_x^2/k_b^2\right)^{(q-1)/2}} & for \quad k_x^2 \geq k_b^2 \end{cases} \qquad (6)$$

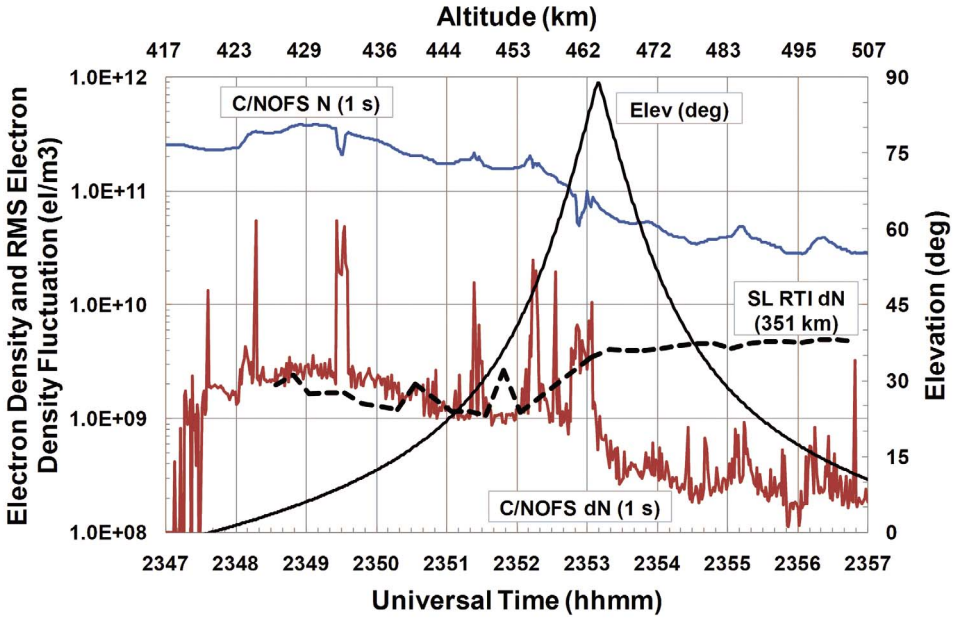

Figure 1. Transit of the C/NOFS satellite over São Luís on 2 December 2008, represented by the altitude values in the upper horizontal line and the elevation curve (which peaks at 235310 UT); 1 s average and standard deviation of electron density fluctuations detected by the onboard Planar Langmuir Probe (upper curve and lower highly irregular curves, respectively); standard deviation of electron density fluctuations estimated from the São Luís radar data for the altitude of 351 km (thick dashed curve). The altitude and all the curves are functions of Universal Time, and elevation values (electron densities) should be read on the right (left) vertical axis.

that the four-digit representation hhmm UT for Universal Time references indicates that the two rightmost digits ss of the full version hhmmss UT are equal to zero. Indeed, this notation was used in the present paragraph.

[10] The procedures leading to the estimation of values of the spectral shape parameters L_o, L_b, p, and q will be described in more detail with the help of one example. Figure 1 characterizes the C/NOFS satellite transit over São Luís from 2347 UT to 2357 UT on 2 December 2008 by relating the altitude values indicated in the upper horizontal line and the elevation curve (which peaks at 235310 UT) to Universal Time. Elevation values should be read on the right vertical axis. Figure 1 also shows, as functions of Universal Time: (1) the 1 s average (upper curve) and (2) the standard deviation (lower and highly irregular curve) of electron density fluctuations detected by the Planar Langmuir Probe onboard the satellite. These two curves should be associated with the left vertical axis. The thick dashed curve in Figure 1, also associated with Universal Time and the left vertical axis, will be described later.

[11] Figure 2 shows the São Luís coherent scatter radar RTI map of *F* region echoes for 2 December 2008 (using a decibel scale for the *S*/*N* ratio), as well as the position of the C/NOFS satellite at 235310 UT, when the maximum elevation (approximately 89°) with respect to the station was reached. The maximum radar backscatter is observed from 300 km to 350 km. Indeed, during the solar minimum period, the ionosphere collapses and the altitude range from 300 km to 350 km corresponds to the height of the *F* region maximum even near the magnetic equator [*Heelis et al.*, 2010]. It is evident from the horizontal time axes of Figures 1 and 2 that, although radar measurements are performed for hours, radar and C/NOFS PLP observations can only be related during a few minutes around that time instant of maximum elevation. Figure 2 also indicates that the C/NOFS Planar Langmuir Probe was not sampling intense irregularities during this time interval. This observation is consistent with the curve for the 1 s standard deviation of the electron density fluctuations in Figure 1, which exhibits generally small values in comparison with the average value of the same parameter. This curve also displays a small number of very sharp peaks that cannot be observed in Figure 2. Indeed, the low spatial resolution of the radar (induced by a broad beam width and finite pulse length) and the

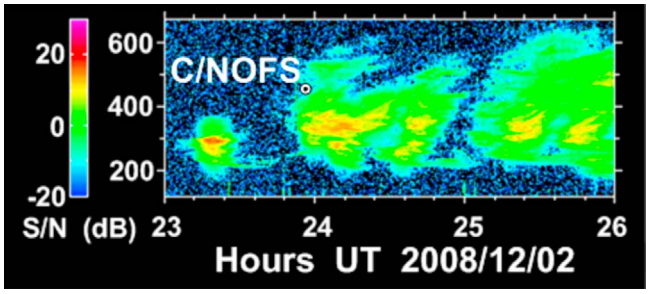

Figure 2. INPE's São Luís coherent scatter radar RTI map of *F* region echoes for 2 December 2008 (using a decibel scale for the *S*/*N* ratio), as well as the position of the C/NOFS satellite at 2353 UT (peak elevation with respect to the station).

relatively long integration time used for processing its raw data produce a strong smoothing effect on fast fluctuations of the *S*/*N* ratio.

[12] Consecutive 4 s batches of high-resolution C/NOFS PLP data (at the sampling rate of 512 Hz) were detrended. That is, a least squares straight line was subtracted from each batch. The power spectral density of each detrended (zero-mean) batch of C/NOFS PLP data was determined using the Maximum Entropy Method [*Fougere*, 1985]. Next, the one-dimensional model (6) was adjusted to each experimental spectra to estimate the values of the associated shape parameters L_o, L_b, p, and q. The results from the application of these procedures to the above C/NOFS PLP data are shown in Figure 3, which repeats the previous altitude and elevation information and also shows the curve of the 4 s standard deviation of the normalized electron density fluctuation $\delta N/N$ (%) as a function of Universal Time. Note that, due to the longer averaging time interval, the present curve is smoother than the corresponding one in Figure 1 and does not display some previously observed intense short-duration peaks that are prominent with respect to the 1 s average background values. For example, the observed peaks at approximately 234815 UT, 235235 UT and 235648 UT in Figure 1 are not seen in Figure 3. It is noted that the spectral index p is relatively uniform in comparison with the other three spectral shape parameters, which fluctuate as functions of Universal Time. However, it should be observed that the scale sizes L_o and L_b reach low values, the spectral index q attains high values, and the three parameters also remain relatively stable during periods of intense electron density fluctuations $\delta N/N$. These observations are extensively applicable to the results from the other listed days.

[13] Finally, the fixed values for the spectral shape parameters L_o = 12.5 km, L_b = 0.08 km, (p-1) = 1.6 and (q-1) = 3.6 have been selected for future scintillation calculations by averaging the results from the application of the described processing to batches corresponding only to intense electron density fluctuations $\delta N/N$ (above 5%). Figure 4 represents the normalized power spectral density model (6) by a thick line, together with MEM spectra corresponding to all the 4 s batches of intense electron density fluctuations indicated above (thin lines). Dispersion of the experimental spectra around the assumed model is evident. However, there is also a good agreement between the model and the average experimental spectra. Additional comments on the selection of fixed spectral shape parameters will be presented at the end of the present section, after the description of the procedure for the estimation of the mean square electron density fluctuation $\langle \Delta N^2 \rangle$.

[14] A full characterization of the power spectral density of the irregularities, necessary for scintillation calculations, also depends on the estimation of the mean square electron density fluctuation $\langle \Delta N^2 \rangle$. In situ C/NOFS PLP data could also be used to estimate values for $\langle \Delta N^2 \rangle$ at the vehicle altitude, but not to provide information on its known variability with height. However, it is well established that, under conditions discussed by several authors [*Woodman and Basu*, 1978; *Walker et al.*, 1987; *Ishimaru*, 1997], easily met in the present case, the *s*/*n* ratio between the received backscattered power from a given volume at a vertical range r and that from sky noise can be estimated with the help of the radar equation for monostatic scattering. Using the three-dimensional spectral density model (1), the following relation between *s*/*n* and $\langle \Delta N^2 \rangle$ can be obtained, as outlined in Appendix A

$$(s/n) = \frac{r_e^2}{32\pi^3 k_B}\left(\frac{G^2 \overline{g}^2 \theta_{3\perp} \delta h_r \lambda_r^3 P_t}{T_{sky} B_N L_{tot}}\right)\left(\frac{\lambda_r^q}{2^q S_1 L_o^{p-2} L_b^{q-p}}\right) \cdot \frac{\langle \Delta N^2 \rangle}{r^2} \approx \frac{r_e^2}{32\pi^3 k_B} C_r C_m \frac{\langle \Delta N^2 \rangle}{r^2} \quad (8)$$

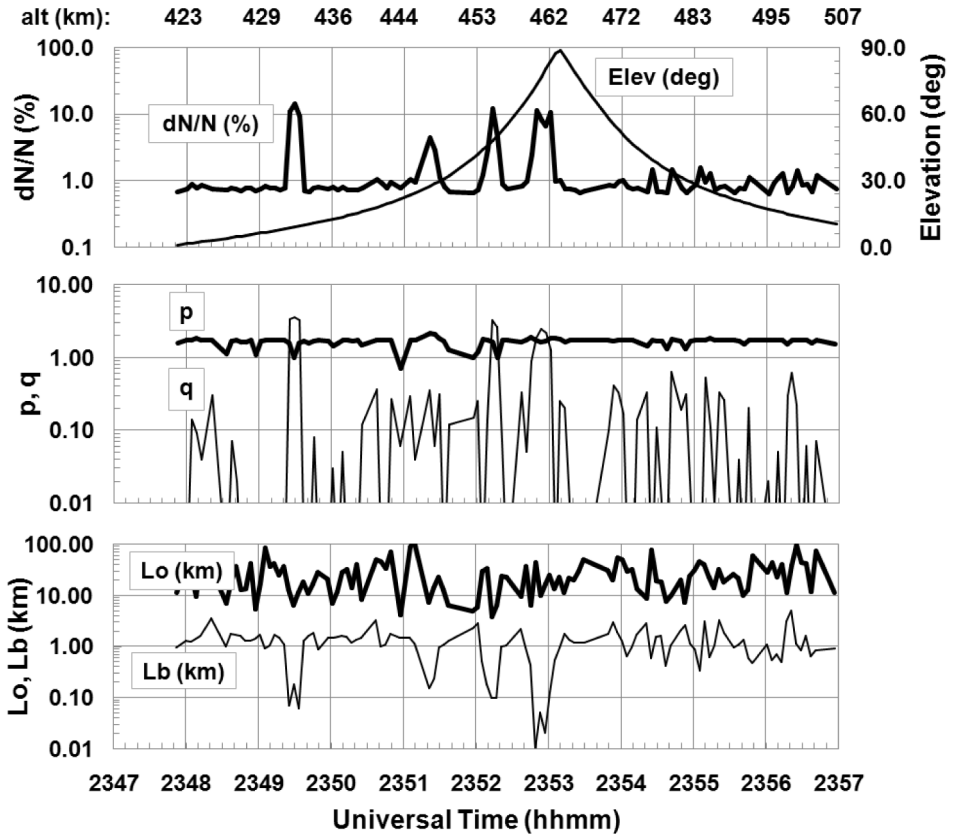

Figure 3. Standard deviation of the normalized electron density fluctuation $\delta N/N$ (%) and shape parameters L_o, L_b, p, and q of the one-dimensional power spectral density model (6) extracted from 4 s batches of detrended high-resolution C/NOFS PLP data for 2 December 2008.

In the above expression, $r_e = 2.8179 \times 10^{-15}$ m is the classical electron radius; $k_B = 1.38 \times 10^{-23}$ J/K is the Boltzmann's constant; G is the antenna gain; $\overline{g}^2$ is the average value of the square of the radiation pattern (spatial power flux distribution normalized to maximum unit value); $\theta_{3\perp}$ is the half-power beam width in the geomagnetic EW plane; δh_r is the radar pulse length; λ_r is the radar wavelength; P_t is the transmitted power; L_{tot} aggregates system and propagation losses; T_{sky} is the sky noise temperature; and B_N is the receiver effective noise bandwidth. The signal-to-noise ratio s/n is inversely proportional to the square of the vertical range and directly proportional to the mean square electron fluctuation $\langle \Delta N^2 \rangle$. It also depends on the terms C_r (which groups parameters of the radar, losses and the sky noise temperature) and C_m (which depends on the parameters which characterize the irregularity volume), defined by the corresponding pairs of parentheses in the above expression. It should be noted that these terms are not independent from each other, since changes of the operating frequency simultaneously affect the radar performance and the scattering properties of the medium, as well as the sky noise temperature.

[15] Using equation (8), an estimate for $\langle \Delta N^2 \rangle$ at each height-dependent radar volume could be obtained from the corresponding s/n measured value, generally displayed in the form of range-time-intensity (RTI) maps, provided that the product $(C_r C_m)$ is known.

[16] Even under favorable conditions, there are uncertainties involved in this process. As remarked by *Hysell et al.* [1994b] and also evident from the derivation in Appendix A, the estimated s/n expression results from several approximations and assumptions. Furthermore, due to the single-slit camera nature of fixed-beam radars, RTI maps derived from radar data would only provide totally accurate representations of the spatial structure of ionospheric irregularities if they remained undistorted while drifting over the radar at a uniform velocity, and if

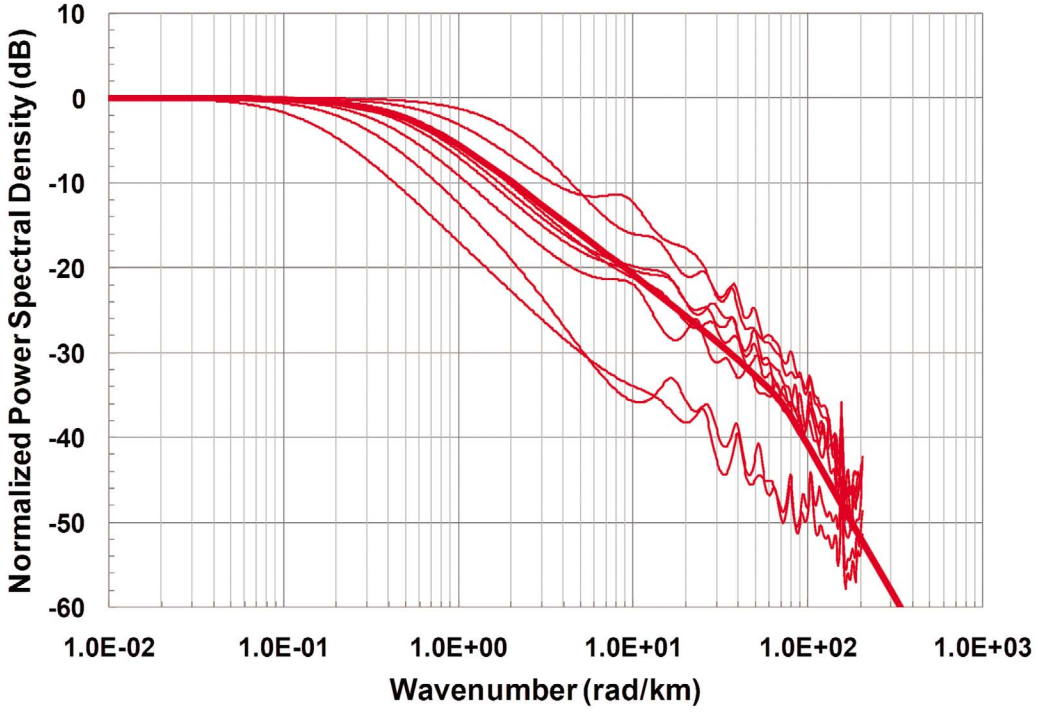

Figure 4. Normalized one-dimensional power spectral density model (6), assuming L_o = 12.50 km ($k_o = 2\pi/L_o$ = 0.50 rad/km), L_b = 0.080 km ($k_b = 2\pi/L_b$ = 78.54 rad/km), (p-1) = 1.6, and (q-1) = 3.6 (thick line), and MEM spectra corresponding to the 4 s batches of intense electron density fluctuations indicated in Figure 3 (thin lines).

the slit were much narrower than the features of interest [*Woodman and LaHoz*, 1976; *Hysell*, 2000; *Woodman*, 2009]. To use equation (8) on a long-term basis, it would be necessary to periodically calibrate the radar (gain, radiation pattern, transmitted power, losses, etc.) to account for aging and maintenance, and to measure the sky noise temperature during irregularity-free evenings. It should be remembered that the evening T_{sky} may rapidly vary during some periods of the year. For example, as reported by *Hysell et al.* [1994b], T_{sky} rose and fell between 6000 K and 15000 K as the galactic center passed through the Cornell University Portable Radar Interferometer (CUPRI) main beam during 3 h evening periods of all days of their July and August 1990 observations of equatorial spread F on Kwajalein. However, this phenomenon was not expected to occur during the days selected for calculations in the next sections.

[17] On the other hand, simultaneous measurements have shown that the enhanced backscattered powers received by coherent scatter radars are related to electron density fluctuations detected by probes on board rockets or satellites [*Kelley et al.*, 1976; *Tsunoda et al.*, 1982]. It is also well accepted that the meter-scale irregularities that are responsible for radar echoes receive energy from the longer scales through cascade processes [*Haerendel*, 1973; *Kelley*, 1989]. Indeed, based on this concept, radar observations of meter-scale irregularities have been used to diagnose larger-scale phenomena [*Woodman*, 2009]. In addition, it has been shown [*Basu et al.*, 1978] that, during approximately 1 h after the onset of equatorial irregularities, the kilometer- and meter-scale irregularities coexist. For the present work, it is particularly relevant to note that *Rodrigues et al.* [2004] recently analyzed simultaneous GPS scintillation records and RTI maps from INPE's São Luís Observatory. They confirmed that, for the highest-elevation satellite, the scintillation index S_4 reached its maximum values when the corresponding signal intercepted the region of the plume producing the strongest radar echoes. Further, in spite of the uncertainties previously listed that also affected their calculations, *Hysell et al.* [1994b] concluded that their prediction of 3 m backscatter based upon the Kwajalein rocket data agreed with the CUPRI observations to within a few decibels. Similar calculations by *Walker et al.* [1987] for typical polar F region conditions and parameters of the Goose Bay radar lead to S/N [= 10 log(s/n)] values

that exceeded 40 dB, while the strongest measured value was 35 dB. However, these authors emphasized that their calculations were idealized, that several loss processes (due to the ionosphere, defocusing, etc.) had been ignored and estimated that, had they been considered, *S*/*N* would have been reduced by 6 dB to 10 dB. These are encouraging results, which suggest that the algorithm using *s*/*n* coherent scatter radar measurements described in the next sections may play a positive role in improving the accuracy of scintillation calculations.

[18] Under the assumption of fixed and known values for the parameters L_o, L_b, p, and q of the power spectral density of the irregularities, the term C_m of equation (8) can be calculated. Rather than using nominal values for the radar parameters and an average value of T_{sky} for the estimation of C_r, which might present the difficulties already discussed, instants of time corresponding to periods of high elevation GPS data were initially selected. Since the GPS receiver and the radar are collocated at INPE's São Luís Observatory, the satellite signals would, in principle, propagate through approximately the same volumes of broadband irregularities being simultaneously sampled by the radar during these periods. Supported by the arguments and evidence listed in the previous paragraph, the algorithm described in section 4 was applied only to the information on the RTI radar maps corresponding to the selected periods and the value of C_r was adjusted to provide a good agreement between average values of measured and calculated S_4. The value of C_r resulting from this course of action remained unchanged during calculations performed for all other elevations. Figure 1 also displays a thick dashed curve for $\langle \Delta N^2 \rangle^{1/2}$ estimated from São Luís coherent scatter radar data for the altitude of 351 km through equation (8). The values along the radar-derived curve are in good agreement with the ones from C/NOFS PLP data between 234830 UT and 235200 UT. Indeed, Figure 2 shows that the two instruments sampled equally weak irregularities at different altitudes during this period. Figure 2 indicates that the radar detected increasingly strong echoes from the altitude of 351 km during the next minute (235200 UT to 235300 UT), which remained at the highest value until 235700 UT, while the C/NOFS satellite continued to orbit through a region of weak irregularities. A closer comparison between the C/NOFS and the radar-derived $\langle \Delta N^2 \rangle^{1/2}$ curves in Figure 1 is difficult, due to the arguments listed in the paragraph immediately above Figure 2. However, the consistency between the two curves supports the application of the procedures based on equation (8) to scintillation calculations.

[19] For forecasting purposes, the procedure to be described contains an inherent and obvious limitation, which should be stressed: while the detection of *F* region structures by coherent scatter radars generally imply scintillation at VHF and UHF frequencies, the opposite is not true. Indeed, *Basu et al.* [1978] established that, approximately 1 h after the onset of the instability process leading to equatorial spread *F*, meter-scale irregularities decay while kilometer-scale ones retain their high spectral intensities. Their observations indicated that irregularity structures detected around midnight could cause significant scintillation even in the *L* band but generally fail to produce any appreciable backscatter [*Basu et al.*, 1988; *Caton et al.*, 2004]. In other words, the procedure will miss existing scintillation events at VHF and UHF frequencies if the effects of meter-scale structures are not represent in the RTI maps.

[20] Figure 5 displays variations of $\langle \Delta N^2 \rangle^{1/2}$ with height estimated from the São Luís coherent scatter radar data for 2400 UT (thin curve) and 2409 UT (thick curve) on 2 December 2008 using the above procedure. Both altitude profiles exhibit decreased values between 450 km and 490 km, which coincide with the altitude range of the C/NOFS satellite during its transit over São Luís, according to Figures 1–3. The altitude profiles additionally show two equally strong slabs of irregularities centered at 350 km and 525 km, with different thicknesses (approximately 170 km and 30 km for the 2400 UT profile and 210 km and 30 km for the 2409 UT profile, respectively). The importance of considering variations of $\langle \Delta N^2 \rangle^{1/2}$ along raypaths in detail, an essential feature of the present model, should be evident from Figure 5. This information is derived from routine radar measurements, which are performed for hours. However, due to its low resolution, the radar data cannot be used to simultaneously estimate the spectral shape parameters L_o, L_b, p, and q. On the other hand, estimation of these parameters from high-resolution C/NOFS PLP data can only be related to simultaneous radar-derived $\langle \Delta N^2 \rangle^{1/2}$ values for a limited altitude range during the few minutes of the satellite transit over the São Luís observatory. Therefore, it is very difficult to take variations of the five spectral parameters along raypaths into account for scintillation calculations during most of the time. The adoption of fixed values for the spectral shape parameters obtained by averaging respective results from periods of intense electron density fluctuations, aimed at circumventing the above difficulties, is based on extensive observations showing that these parameters remain relatively stable during these periods. *Kelley and Livingston* [2003] overlapped power spectral densities resulting from rocket in situ measurements performed during equatorial spread *F* conditions at different launch sites, showing that they are basically identical. To a certain extent, this also supports the use of fixed values for the parameters L_o, L_b, p, and q in the calculations to be described in the following sections. It is clear from Figure 3 that this assumption is not valid for weak electron density fluctuations, which display more variable spectral shape parameters. However, weak irregularities are expected

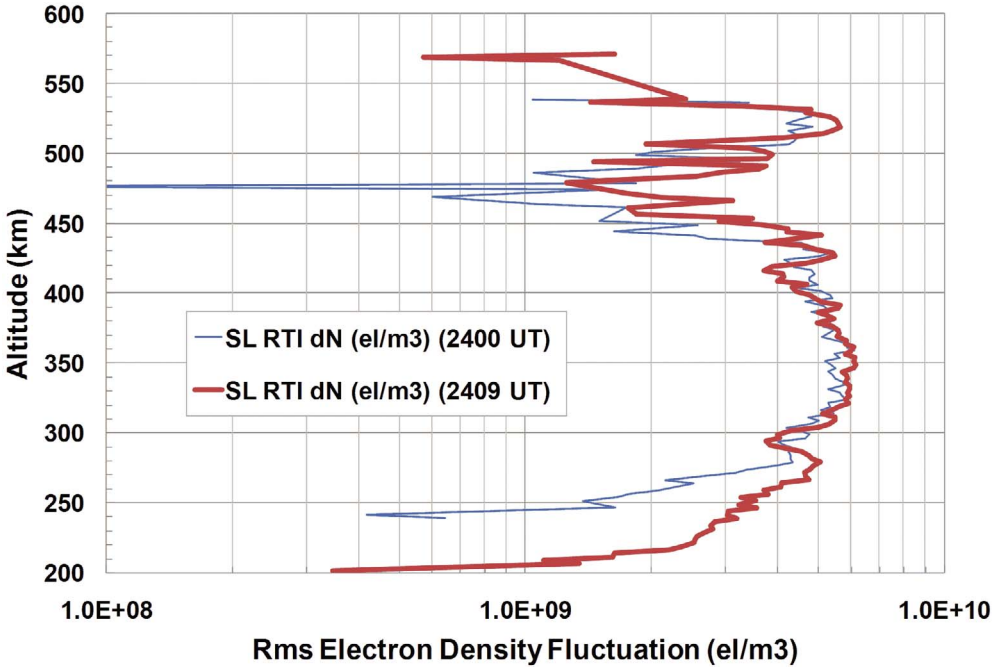

Figure 5. Variations of $\langle \Delta N^2 \rangle^{1/2}$ with height estimated from the São Luís coherent scatter radar data for 2400 UT (thin curve) and 2409 UT (thick curve) on 2 December 2008.

to play a secondary role in ionospheric scintillation. Finally, it is acknowledged that the assumption of fixed values for the spectral shape parameters also contributes to prediction errors by the present model.

3. Slant Propagation Through an Irregularity Layer

[21] The slant propagation of a plane wave through a three-dimensional irregularity layer in the equatorial ionosphere will be represented with basis on a reference frame with origin at the receiver, located on the ground, the y axis aligned with the horizontal magnetic field line direction and the z axis pointed upward. The propagation direction will be characterized by the unit vector (d_x, d_y, d_z) aligned with the slant raypath.

[22] The irregularity layer will be represented by a large number of horizontal rectangular screens uniformly spaced in height, each centered at the raypath and with sides parallel to the x and y axes, respectively. The constant spacing between consecutive screens will be denoted by δz, the heights of the screens by $z_j = z_{max} - j\delta z$ ($j = 0, \ldots, J$), where z_{max} is the upper height of the irregularity layer, and a uniform grid with basic lengths (δx, δy) will be defined over each of them.

[23] As described in Appendix B, propagation from the top to the bottom of the irregularity layer can be represented by repeated application of the equation

$$u_{m,n}(z-\delta z) = \exp\left[-i\frac{r_e \lambda \delta z}{d_z}\delta N_{m,n}(z-\delta z)\right] \cdot \sum_{R=-R_M}^{R_M}\sum_{S=-S_M}^{S_M} C_R^x C_S^y u_{m-R,n-S}(z) \quad (9)$$

where $u_{m,n}(z)$ ($-R_M \le m \le R_M$, $-S_M \le n \le S_M$) is the complex amplitude value of the field at the node (m, n) of the horizontal grid located at height z. Initially, at the top z_{max} of the irregularity layer, all these values are equal to one. For each propagation step (that is, for each height z), a random vector $\delta N_{m,0}(z-\delta z)$ ($-R_M \le m \le R_M$) is specified in conformity with the inverse Fourier transform of the square root of the one-dimensional power spectral density (6), assuming the fixed values for the parameters L_o = 12.5 km, L_b = 0.08 km, (p-1) = 1.6 and (q-1) = 3.6, but with $\langle \Delta N^2 \rangle$ estimated through expression (8) from the measured s/n value for the corresponding height. The corresponding phase spectrum of the irregularities is represented by a vector of mutually independent random variables uniformly distributed between 0 and 2π. The present specification, only adopted in the absence of

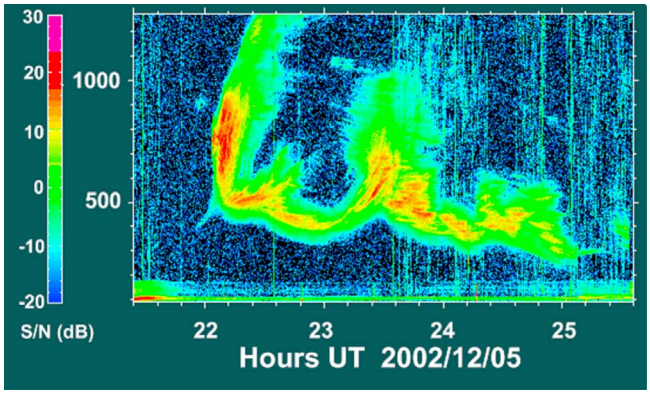

Figure 6. INPE's São Luís radar RTI map of *F* region echoes for 5 December 2002 (using a decibel scale for the *S*/*N* ratio).

well-accepted models for the generation of observed asymmetric structures with steep edges [*Dyson et al.*, 1974; *Kelley et al.*, 1976; *Costa and Kelley*, 1978; *Rino et al.*, 1981; *Basu et al.*, 1983; *Hysell et al.*, 1994a], could have an impact on the calculation of the scintillation index S_4, as discussed by *Costa and Basu* [2002]. Field alignment of the irregularities is then forced by equating $\delta N_{m,n}(z-\delta z) = \delta N_{m,0}(z-\delta z)$ ($-R_M \le m \le R_M$, $-S_M \le n \le S_M$). Additionally,

$$C_0^x = 1 + 2[c_1(\beta_x) - c_0(\beta_x)] \tag{10}$$

$$C_R^x = c_{R+1}(\beta_x) - 2c_R(\beta_x) + c_{R-1}(\beta_x) \tag{11}$$

$$\beta_x = 2\sqrt{d_z}\left(\delta x / z_f\right) \tag{12}$$

$z_f = (2\lambda\,\delta z)^{1/2}$ is the Fresnel scale size, λ is the wavelength of the transmitted signal and

$$\begin{aligned} c_q(\beta) = {} & \frac{1}{\sqrt{2i\pi\beta}}\left\{[\pi(\beta q) f(\beta q) - 1]\sin\left[\frac{\pi}{2}(\beta q)^2\right]\right. \\ & \left. - [\pi(\beta q) g(\beta q)]\cos\left[\frac{\pi}{2}(\beta q)^2\right]\right\} \\ & - \frac{i}{\sqrt{2i\pi\beta}}\left\{[\pi(\beta q) f(\beta q) - 1]\cos\left[\frac{\pi}{2}(\beta q)^2\right]\right. \\ & \left. + [\pi(\beta q) g(\beta q)]\sin\left[\frac{\pi}{2}(\beta q)^2\right]\right\} \end{aligned} \tag{13}$$

In equation (13), $f(\beta q)$ and $g(\beta q)$ are the auxiliary functions associated with the Fresnel integrals [*Abramowitz and Stegun*, 1972]. The expressions for C_S^y can be obtained from those for C_R^x by trivial changes of indices and the symbols (q, β) in equation (13) stand for both (R, β_x) and (S, β_y).

[24] Finally, equation (9) should be applied once more with $\delta N_{m,n}(0) = 0$ and $z = \delta z = z_{\min}$, where $z_{\min} = z_{\max} - J\delta z$ is the height of the bottom of the layer, to produce the field on the ground.

4. Results From Calculations Using RTI and Scintillation Data From INPE's São Luís Observatory

[25] The equatorial ionospheric scintillation model to be described, based on the algorithms specified in the previous sections, has been applied to data from the 30 MHz coherent scatter ionospheric radar located at INPE's São Luís Observatory. A brief description of the radar system, conceptually similar to the Jicamarca Unattended Long-term Investigations of the Ionosphere and Atmosphere (JULIA) radar [*Hysell and Burcham*, 1998], can be found in the recent literature [*de Paula and Hysell*, 2004; *Rodrigues et al.*, 2008]. Figure 6 shows a range-time-intensity (RTI) radar map obtained from measured backscattered signals from *F* region ionospheric irregularities on 5 December 2002, using a decibel scale for the *S*/*N* ratio. Additional examples of INPE's São Luís radar RTI maps can be seen in the above references, as well as in the work by *Rodrigues et al.* [2004]. For the present study, RTI data were also available from the evenings of 16 November 2001, 28 December 2001, 6 October 2002, 16 October 2002, and 1 December 2002, in addition to those corresponding to Figure 6. It should be observed that geomagnetically quiet days have been selected, with 3-hourly Kp-index values below 4o, but with 10.7 cm (2800 MHz) solar radio flux density over 210 sfu for the 2001 days and approximately equal to 160 sfu for the 2002 days (1 solar flux unit equal to 10^{-22} W/m^2/Hz). As exemplified by

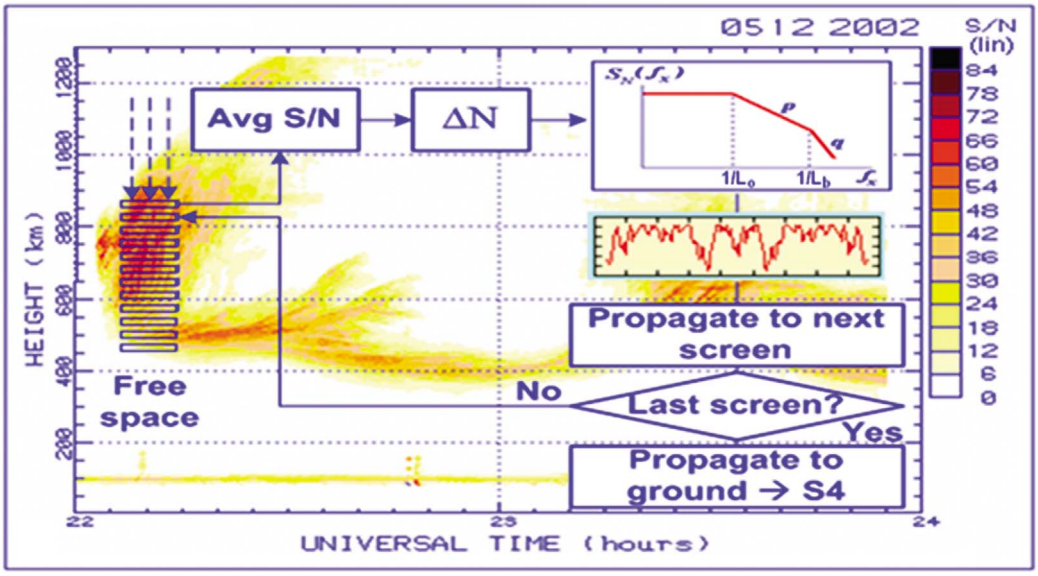

Figure 7. Flowchart of the complete three-dimensional model, combining the generation of electron density fluctuations and the radio wave propagation algorithm, with the RTI map from the São Luís coherent scatter data for 5 December 2002 in the background.

Figures 2 and 6, strong radar echoes due to 5 m irregularities can be observed during solar maximum (5 December 2002) or minimum (2 December 2008) periods. However, they more frequently occur and reach increased altitudes during solar maximum than during solar minimum periods, all the other geophysical conditions remaining unchanged.

[26] Simultaneous measurements of amplitude scintillation of Global Positioning System (GPS) L1 signals (f_{L1} = 1575.42 MHz) were also performed. Scintillation index S_4 values were determined every minute (from 3000 amplitude samples) for all tracked satellites. It is clear that coherent scatter radar data play an essential role in the present propagation model and that calculation results should be compared with measurements performed by the collocated scintillation monitor. The fact that both instruments are deployed at São Luís, which is very close to the magnetic equator, imposes a natural limitation on the values of the GPS scintillation index S_4 associated with magnetically quiet conditions. Indeed, statistical studies by *de Paula et al.* [2003] and the examples reported by *Muella et al.* [2010] indicate that, while scintillation can be intense around the southern equatorial ionization anomaly crest (with S_4 reaching saturation values at the L1 frequency), it is weak over the magnetic equator. The measured scintillation index S_4 at São Luís rarely exceeds 0.4 at the same frequency for a lower elevation mask of 30°.

[27] It has been assumed in the calculations that the structures in the RTI map are field-aligned and undergo frozen drift over the radar according with a simple climatological pattern, independent of height, which is consistent with airglow measurements [*Santana et al.*, 2001; *Arruda et al.*, 2006]: v_{Dwe} = 150 m/s for UT < 23 h, with a linear decrease such that v_{Dwe} = 80 m/s at UT = 04 h of the following day. Therefore, for each Universal Time of interest, the model updates the position of the RTI map with respect to the radar, as well as the positions of the GPS satellites, using the azimuths and elevations of their raypaths. Next, as sketched in the flowchart of Figure 7, independent vectors of $(s/n)_j$ values are determined from the RTI map for equally spaced screens located at heights z_j and centered at each raypath, and converted into $\langle \Delta N^2 \rangle_j$ values using equation (8). The procedures described in section 3 are then repeatedly applied for each height to specify the electron density fluctuations $\delta N_{m,n}(z_j - \delta z)$ at the nodes of each screen and to propagate a wave between consecutive screens from the top to the bottom of irregularity layer. Finally, the algorithm is applied once more under free-space conditions from the bottom of the layer to the ground, to determine the received signal and calculate the S_4 value for the corresponding GPS satellite at the Universal Time.

[28] Selected examples of good agreement between S_4 calculations and measurements as functions of Universal

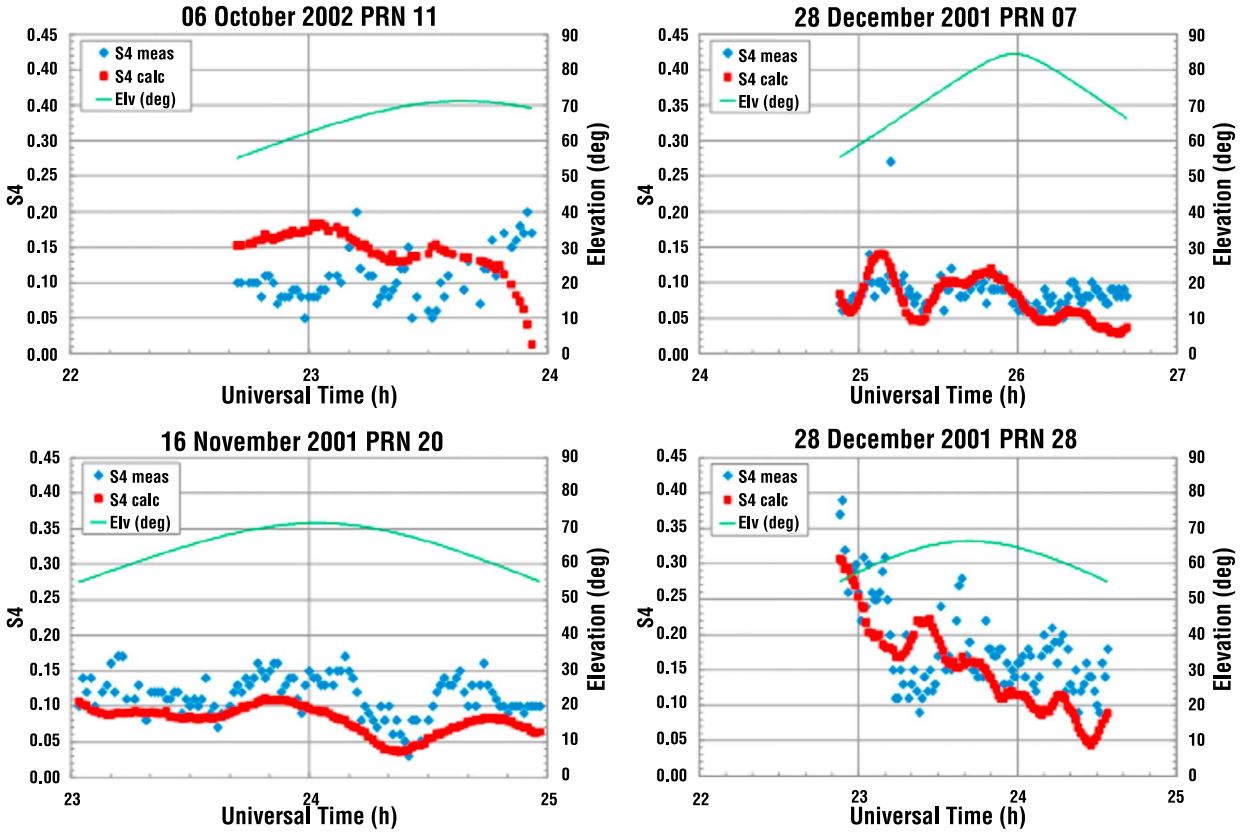

Figure 8. Examples of good agreement between S_4 calculations and measurements as functions of Universal Time. The elevations of the corresponding GPS satellites are also shown.

Time are shown in Figure 8 for different evenings and GPS satellites, together with the elevations of the corresponding raypaths. It should be observed that, as discussed above, Figure 8 covers the full range of low to moderate levels of S_4 typically recorded at the equatorial-latitude station of São Luís for scintillation at the L1 GPS frequency, even during conditions of maximum solar activity. In spite of the use of a climatological model to characterize the drift velocity of irregularity structures through the radar main beam, the time fluctuations of the calculated and measured S_4 values are reasonably well synchronized. It seems realistic to expect improved agreement from future calculations using simultaneously measured drift velocities, unavailable for the present study.

[29] The scatterplot in Figure 9 displays the ratio S_{4meas}/S_{4calc} between measured and calculated S_4 values as a function of elevation of the raypath for the complete data set of 1705 samples, which also includes those that do not reach the good agreement observed in Figure 8. To provide an expanded view of the S_{4meas}/S_{4calc} ratio distribution, the vertical axis has been limited to the maximum value of six, clipping 26 samples. It is interesting to use the elevation as a basis for this comparison since, as explained previously, GPS signals from high elevation satellites propagate through approximately the same irregularities being simultaneously sampled by the radar. On the other hand, as the elevation decreases, the corresponding raypaths would intercept structures that are farther away from the radar beam. Due to the actual time evolution of irregularities and to more complex drift patterns than the one considered here, diffractive patterns traversed by lower-elevation raypath may differ from those resulting from the combination of radar observations and extrapolations by the frozen in assumption. Therefore, degradation in the agreement between S_4 calculations and measurements is expected as the elevation of the raypath decreases. Indeed, structures initially located at an altitude of 500 km along the vertical axis of the radar beam would have drifted east for 350 km during

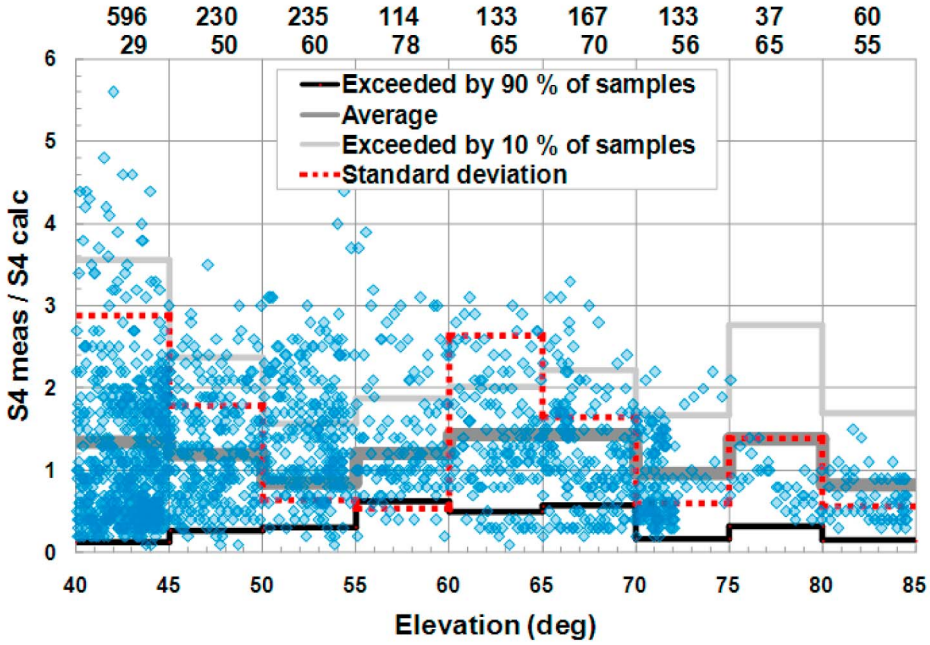

Figure 9. Ratio S_{4meas}/S_{4calc} as a function of elevation for the complete data set of 1705 samples. The lower (black) line indicates, for 5 degree elevation classes, values that are exceeded by 90% of the samples. The upper (light gray) line indicates, for the same classes, values that are exceeded by 10% of the samples. The central continuous (thick gray) and square-dotted lines indicate the average ratio and the corresponding standard deviation for each class, respectively. The upper and lower rows of figures at the top of the plot indicate, for each class, the number of samples and the percentage of samples in the interval (0.5, 1.5), respectively.

approximately 40 min to reach the elevation of 55°, experiencing "internal changes" due to decay and more complex drift patterns.

[30] Figure 9 provides an extensive and detailed picture of the agreement that can be reached between the results from the present calculations and the corresponding measurements. The upper (light gray) line indicates, for 5 degree classes in elevation, ratios that are exceeded by 10% of the samples. The lower (black) line indicates, for the same classes, ratios that are exceeded by 90% of the samples. Additionally, the central continuous (thick gray) line indicates the average ratio for each class and the square-dotted line the corresponding standard deviation. The upper row of figures on top of Figure 9 indicates the number of samples in each class. It should be observed that the number of samples in the class of elevations (75°, 80°) is small. Only four points characterize the 10% highest values of the ratio S_{4meas}/S_{4calc}, and the fifth highest ratio is 1.7. It is possible that an increase in the size of this class could lead to a decrease in the ratio exceeded for 10% of samples to a value more consistent with those of the classes immediately below and above. It is also noted that the average values of the ratios for all classes are constrained to the interval (0.82, 1.43) and that the standard deviations of most classes for elevations above 50° are included in the interval (0.54, 1.64). The lower row of numbers on top of the plot indicates, for each class, the percentage of samples in the interval (0.5, 1.5). The scatterplot and these numbers indicate that, for elevations above 50°, $0.5 \leq S_{4meas}/S_{4calc} \leq 1.5$ for 64% of the samples. However, as expected, degradation in the agreement between calculations and measurements, indicated by an increase in the standard deviation, a decrease in the percentage of samples in the interval (0.5, 1.5) and by a widening of the interval between the 10% and 90% lines, is observed as the elevation decreases.

[31] The format of Figure 9 effectively illustrates the role of the elevation angle on the agreement between calculated and measured values of S_4. However, the ratio S_{4meas}/S_{4calc} does not allow one to observe the level of agreement that can be reached throughout the range of S_4 values typically measured by the São Luís scintillation

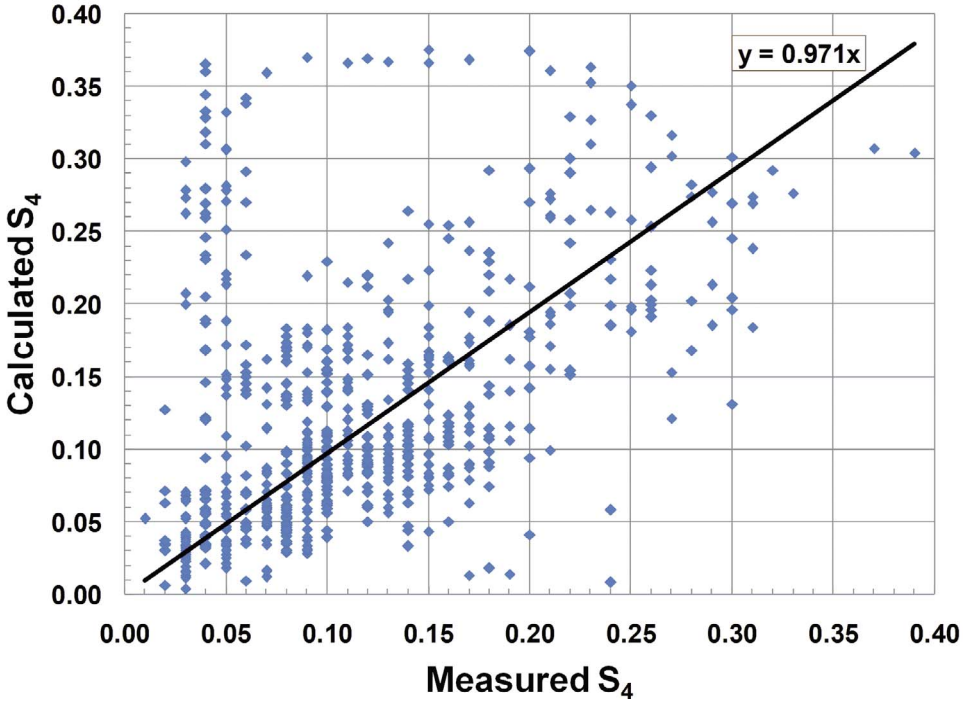

Figure 10. Comparison between all the 644 pairs of calculated and measured S_4 values associated with elevations above 55° and corresponding least squares trend line through the origin.

monitor. This can only be done by a direct comparison between absolute values (and not by their ratios). Hence, all the 644 pairs of calculated and measured S_4 values associated with elevations above 55° are compared in Figure 10. It is observed that the resulting least squares trend line through the origin is very close to the ideal one (y = x) and that most of the points are evenly spread around it within the entire interval $0 < S_4 < 0.4$. The exceptions are the outlier ones around $S_{4meas} \approx 0.04$ with $S_{4calc} > 0.2$ and $S_{4calc} \approx 0.37$.

5. Summary

[32] This work described a model for equatorial ionospheric scintillation calculations that took the vertical structure of the irregularities into detailed consideration. The model assumed that structures displayed in RTI maps by the São Luís coherent scatter radar were frozen to the background medium and drifted according to a climatological model. At each time step, the positions of the GPS satellites and the structures were updated. Then, the procedure transformed s/n values observed at a given height along a raypath into $\langle \Delta N^2 \rangle$ Together with fixed spectral shape parameters L_o, L_b, p, and q, estimated from C/NOFS PLP data, it specified random electron density fluctuations at this height, in conformity with an assumed model for their power spectral density. The fields at lower heights and at the ground were obtained by repeated application of the combination of this specification with a propagation algorithm.

[33] A close and extensive comparison between results from S_4 calculations and measurements performed at the L1 GPS frequency was presented, using two different formats. First, selected examples of good agreement between calculations and measurements were displayed as functions of Universal Time. In spite of the use of a climatological model to characterize the drift velocity of irregularity structures through the radar main beam, the time fluctuations of the calculated and measured S_4 values were reasonably well synchronized. A scatterplot displaying the ratio between measured and calculated S_4 values as a function of elevation of the raypath for the complete data set was also presented and discussed, displaying an encouraging agreement between the results from the current calculations and the corresponding measurements.

[34] It is evident that the described formulation relied on coherent scatter radar data more intensively than on C/NOFS in situ data. Future work will reverse these roles, by extracting both spectral shape parameters L_o,

L_b, p, and q, as well as $\langle \Delta N^2 \rangle$ in real time from C/NOFS PLP measurements during near-overhead orbits over São Luís. That is, the spectral shape parameters will be allowed to vary according to observations. A comparison between $\langle \Delta N^2 \rangle$ and simultaneous coherent scatter radar measurements of s/n from the same region of the C/NOFS satellite should be tested as an alternative estimation technique for the parameter C_r in equation (8). Additionally, data from simultaneous C/NOFS, radar or space-receiver drift velocity measurements, unavailable for the present work, should be used in the place of the assumed climatological model. In principle, this more realistic and flexible model has potential to improve scintillation predictions with respect to the present formulation and should also be extended to other frequencies of interest.

Appendix A: Backscattered Power From an Irregularity Volume

[35] It is well known [*Walker et al.*, 1987; *Ishimaru*, 1997] that the received power s resulting from the incidence of an electromagnetic field upon a given irregularity volume can be estimated with the help of the radar equation for monostatic scattering.

$$s = \left(\frac{\lambda_r}{4\pi}\right)^2 G^2 P_t \iiint_V \frac{g^2(\hat{R})}{L_{tot} R^4} \left[r_e^2 S_N^{3D}(2k_r \hat{R})\right] dV \qquad \text{(A1)}$$

where the term within square brackets is the differential cross section (backscattered power per unit solid angle, per unit incident power flux) per unit volume of a scatterer; $\vec{R}$ is the position vector of the corresponding elementary volume (origin at the center of the radar antenna), $R = |\vec{R}|$ and $\hat{R} = \vec{R}/R$ are the associated slant range and unit vector, respectively; G is the antenna gain; $g(\hat{R})$ represents the radiation pattern (spatial power flux distribution normalized to maximum unit value); P_t is the transmitted power; L_{tot} aggregates system and propagation losses; $k_r = 2\pi/\lambda_r$ and λ_r are the radar wave number and wavelength, respectively; $r_e = 2.8179 \times 10^{-15}$ m is the classical electron radius; and V is the sampled volume, centered at the vertical range r and approximately limited by the antenna main beam and the pulse length δh_r. That is,

$$s = \left(\frac{r_e \lambda_r}{4\pi}\right)^2 G^2 P_t \int_{-r\theta_{3\perp}/2}^{r\theta_{3\perp}/2} \int_{-r\theta_{3ll}/2}^{r\theta_{3ll}/2} \int_{r-\delta h_r/2}^{r+\delta h_r/2} \frac{g^2(\hat{R})}{L_{tot} R^4} \cdot S_N^{3D}\left(2k_r \frac{x}{R}, 2k_r \frac{y}{R}, 2k_r \frac{z}{R}\right) dx dy dz \qquad \text{(A2)}$$

In the above expression, θ_{3ll} and $\theta_{3\perp}$ are the half-power beam widths in the geomagnetic NS and EW planes, respectively. Next, this expression will be simplified, considering the appropriate parameters ($f = 30$ MHz, $\lambda_r = 10$ m, $\theta_{3\perp} \approx 10°$, $\theta_{3ll} \approx 20°$, $\delta h_r \approx 2.5$ km) for the São Luís coherent scatter radar [*de Paula and Hysell*, 2004; *Rodrigues et al.*, 2004]. Note that, in comparison with the very fast variations experienced by the power spectral density (due to the exponential and power laws), $g(\hat{R})$, R and L_{tot} remain approximately constant within the volume and can be extracted from the integral. Using the additional approximations $R \approx$ r and $z/R \approx$ r/R ≈ 1, expression (A2) becomes

$$s = \left(\frac{r_e \lambda_r}{4\pi}\right)^2 \frac{G^2 \overline{g}^2 \delta h_r P_t}{L_{tot}} \frac{1}{r^2} \cdot \int_{-\theta_{3\perp}/2}^{\theta_{3\perp}/2} \int_{-\theta_{3ll}/2}^{\theta_{3ll}/2} S_N^{3D}(2k_r\xi, 2k_r\zeta, 2k_r) d\xi d\zeta \qquad \text{(A3)}$$

where $\overline{g}^2$ is the average value of $g^2(\hat{R})$ within the main beam. Note that, for the arguments in equation (26), $k_\perp^2 = k_x^2 + k_z^2 = (2k_r)^2 (1 + \xi^2) > k_b^2$, indicating that only the lower part of expression (2), in combination with expression (1), should be used in the estimation of the received power s. After straightforward manipulations, expression (A3) can be written in the form

$$s = \frac{\sqrt{\pi} r_e^2}{32\pi^4} \frac{G^2 \overline{g}^2 \delta h_r \lambda_r^{q+3} P_t}{L_{tot}} \frac{1}{r^2} \frac{\langle \Delta N^2 \rangle}{2^q S_1 L_o^{p-2} L_b^{q-p}} \cdot \int_{-\theta_{3\perp}/2}^{\theta_{3\perp}/2} \left(\int_{-t_o}^{t_o} e^{-t^2} dt \right) \frac{d\xi}{(1+\xi^2)^{q/2}} \qquad \text{(A4)}$$

where $1 \le (1 + \xi^2) \le (1 + \theta_{3\perp}^2/4) \approx 1.0076$ and

$$t_o = \frac{a \left(\frac{2k_r}{k_o}\right)^{\frac{\theta_{3ll}}{2}}}{\left[1 + \left(\frac{2k_r}{k_o}\right)^2 (1 + \xi^2)\right]^{1/2}} \approx a \frac{\theta_{3ll}}{2} \approx 0.174a \qquad \text{(A5)}$$

Therefore, for $a > 11$, it is justified to extend the limits of the inner integral to $\pm\infty$, with the corresponding error being less than 1%. Considering also that the outer integrand is approximately equal to one throughout the interval $(-\theta_{3\perp}/2, \theta_{3\perp}/2)$, expression (8) is obtained for the

signal-to-noise ratio s/n between the received backscattered power s and the sky noise power n.

Appendix B: Algorithm for the Slant Propagation of a Radio Wave Through an Irregularity Layer

[36] The slant propagation of a plane wave through a three-dimensional irregularity layer can be represented by the wave equation

$$\frac{\partial^2 U}{\partial x^2}+\frac{\partial^2 U}{\partial y^2}+\frac{\partial^2 U}{\partial z^2}+k^2\eta^2 U=0 \tag{B1}$$

In the above equation, k is the free space wave number and η is the refractive index of the medium. The y axis is aligned with the horizontal magnetic field line direction and the z axis points upward. The origin is assumed at the receiver, located on the ground. Without any loss of generality, the field $U(x, y, z)$ can be represented by the product of a complex amplitude $u(x, y, z)$ and a phase term

$$U(x,y,z)=u(x,y,z)e^{ik\left(d_x x+d_y y+d_z z\right)} \tag{B2}$$

where (d_x, d_y, d_z) is the unit vector aligned with the slant propagation direction. Substituting the right hand side of equation (B2) for U into equation (B1) and assuming that the scale size of the vertical fluctuations of the complex amplitude u is large in comparison with $|2k\ d_z|^{-1}$, one gets

$$\frac{\partial^2 u}{\partial x^2}+\frac{\partial^2 u}{\partial y^2}+2ik\left(d_x\frac{\partial u}{\partial x}+d_y\frac{\partial u}{\partial y}+d_z\frac{\partial u}{\partial z}\right)+k^2\left(\eta^2-1\right)u=0 \tag{B3}$$

Under the above approximation, the second derivative of u with respect to z becomes much smaller than the fifth term in equation (B3) and can be neglected. This approximation is reasonable for sufficiently high frequencies and small zenith angles. It is seen that the slant propagation of the plane wave is now represented by a parabolic equation, indicating that backscattering has been neglected.

[37] The Fourier split-step algorithm [*Kuttler and Dockery*, 1991] can be used to numerically solve equation (B3). This algorithm assumes that $u(x, y, z)$ is specified at the top of the layer, subdivides it into multiple thin horizontal slabs with common thickness δz and substitutes the Fourier representation

$$u(x,y,z)=\frac{1}{(2\pi)^2}\int_{-\infty}^{+\infty}\int_{-\infty}^{+\infty}\tilde{u}(p,q,z)e^{i(px+qy)}dpdq \tag{B4}$$

into equation (B3) to obtain

$$\frac{\partial\tilde{u}}{\partial z}+\frac{k^2(\eta^2-1)-2k\left(d_x p+d_y q\right)-\left(p^2+q^2\right)}{2ik\ d_z}\tilde{u}=0 \tag{B5}$$

Equation (B5) yields

$$\tilde{u}(p,q,z-\delta z)=\tilde{u}(p,q,z)\ e^{i\frac{k\left(\eta^2-1\right)}{2d_z}\delta z}e^{-i\frac{\left(p^2+q^2\right)+2k\left(d_x p+d_y q\right)}{2k\ d_z}\delta z} \tag{B6}$$

Calculating the inverse Fourier transform of the above equation, it follows that

$$u\left(x+\frac{d_x}{d_z}\delta z,x+\frac{d_y}{d_z}\delta z,z-\delta z\right)=e^{i\frac{k\left(\eta^2-1\right)}{2d_z}\delta z}\cdot\left\{\frac{k\ d_z}{i2\pi\ \delta z}\int_{-\infty}^{+\infty}\int_{-\infty}^{+\infty}u(x',y',z)\ e^{i\frac{k\ d_z}{2\delta z}\left[(x-x')^2+(y-y')^2\right]}dx'dy'\right\} \tag{B7}$$

Each step in the solution of the parabolic equation by the Fourier split-step algorithm begins with the application of the Huygens-Fresnel diffraction integral within curly brackets [*Goodman*, 1968] to the field at the top of each slab. A phase shift depending on the refractive index of the medium and a displacement are then performed to produce the field at the bottom of the same slab. Note that phase shifts and the displacements are not necessary when $\eta = 1$ and $\theta = 0°$, respectively. Equation (B7) should be repeatedly applied to propagate the field from the top to the bottom of the layer. It should then be applied once more with $\delta z = h$, where h is the height of the bottom of the layer, and $\eta = 1$ to produce the field on the ground.

[38] It should be remarked that the phase-screen theory is a particular case of the above development. The final expression for the continuous version of this theory is obtained from equation (B7), again assuming $\delta z = h$ (the height of the single screen), and $\eta = 1$, as well as $u(x', y', h) = \exp[i\varphi(x', y')]$, where $\varphi(x', y')$ is the phase of the screen, proportional to TEC fluctuations. Additionally, it is noted for future reference that the integral in equation (B7) can be analytically integrated in the special case $u(x', y', z) = 1$, showing that the absolute value of the term within curly brackets also becomes equal to one.

[39] The term within curly brackets in equation (B7), denoted $v(x, y, z; \delta z)$, represents a continuous convolution between two functions. A discrete version of this term can be obtained by initially normalizing the variables x, x', y, and y' by uniform horizontal sampling intervals δx and δy, respectively. That is, the changes of variables $x = m\ \delta x$, $x' = \xi\ \delta x$, $y = n\ \delta y$, and $y' = \zeta\ \delta y$ will be introduced

into equation (B7) and the result will be written as a double summation of integrals over unit (ξ, ζ) squares, as follows

$$v_{m,n}(z;\delta z) = \sqrt{\frac{\gamma_x}{i\pi}}\sqrt{\frac{\gamma_y}{i\pi}} \sum_{r=-\infty}^{+\infty}\sum_{s=-\infty}^{+\infty} \int_{r}^{r+1}\int_{s}^{s+1} u(\xi,\zeta,z) \cdot e^{i\left[\gamma_x(m-\xi)^2+\gamma_y(n-\zeta)^2\right]}\, d\xi d\zeta \tag{B8}$$

In the above equation, m, n, r, and s are arbitrary integer indices, $\gamma_x = 2\pi\, d_z\, (\delta x/z_f)^2$, $\gamma_y = 2\pi\, d_z\, (\delta y/z_f)^2$, where $z_f = (2\lambda\ \delta z)^{1/2}$ is the Fresnel scale size and λ is the wavelength of the transmitted signal. Next, $u(\xi, \zeta, z)$ will be approximated by a bilinear function of the first two variables inside each unit square $r \le \xi \le r+1$, $s \le \zeta \le s+1$, with break points at its integer values. That is,

$$\begin{aligned} u(\xi,\zeta,z) = {} & (r+1-\xi)(s+1-\zeta)u_{r,s} \\ & + (\xi-r)(s+1-\zeta)u_{r+1,s} + \\ & + (\xi-r)(\zeta-s)u_{r+1,s+1} + (r+1-\xi) \\ & \cdot (\zeta-s)u_{r,s+1} \end{aligned} \tag{B9}$$

To further simplify notation, the fact that the samples $u_{r,s}$, $u_{r+1,s}$, $u_{r+1,s+1}$, and $u_{r,s+1}$ are obtained at the altitude z has been omitted in expression (B9). Substituting its right-hand side for $u(\xi, \zeta, z)$ into equation (B8), a straightforward calculation leads to

$$\begin{aligned} v_{m,n}(z;\delta z) = {} & \tfrac{1}{2i}\sum_{r=-\infty}^{+\infty}\sum_{s=-\infty}^{+\infty}\left[(m-r-1)I^{1x}_{m-r} - J^{2x}_{m-r}\right]\left[(n-s-1)I^{1y}_{n-s} - J^{2y}_{n-s}\right]u_{r,s} - \\ & -\tfrac{1}{2i}\sum_{r=-\infty}^{+\infty}\sum_{s=-\infty}^{+\infty}\left[(m-r)I^{1x}_{m-r} - J^{2x}_{m-r}\right]\left[(n-s-1)I^{1y}_{n-s} - J^{2y}_{n-s}\right]u_{r+1,s} - \\ & -\tfrac{1}{2i}\sum_{r=-\infty}^{+\infty}\sum_{s=-\infty}^{+\infty}\left[(m-r-1)I^{1x}_{m-r} - J^{2x}_{m-r}\right]\left[(n-s)I^{1y}_{n-s} - J^{2y}_{n-s}\right]u_{r,s+1} + \\ & +\tfrac{1}{2i}\sum_{r=-\infty}^{+\infty}\sum_{s=-\infty}^{+\infty}\left[(m-r)I^{1x}_{m-r} - J^{2x}_{m-r}\right]\left[(n-s)I^{1y}_{n-s} - J^{2y}_{n-s}\right]u_{r+1,s+1} \end{aligned} \tag{B10}$$

where

$$I^{1x}_{m-r} = \sqrt{\frac{2\gamma_x}{\pi}}\int_{r}^{r+1} e^{i\gamma_x(m-\xi)^2}d\xi = \int_{\beta_x(m-r-1)}^{\beta_x(m-r)} e^{i\frac{\pi}{2}t^2}dt \tag{B11}$$

$$J^{2x}_{m-r} = \sqrt{\frac{2\gamma_x}{\pi}}\int_{r}^{r+1}(m-\xi)e^{i\gamma_x(m-\xi)^2}d\xi = \frac{1}{\beta_x}\int_{\beta_x(m-r-1)}^{\beta_x(m-r)} t\, e^{i\frac{\pi}{2}t^2}dt \tag{B12}$$

and

$$\beta_x = \sqrt{2\gamma_x/\pi} = 2\sqrt{d_z}\left(\delta x/z_f\right) \tag{B13}$$

Note that I^{1x}_{m-r} can be expressed in terms of Fresnel integrals and that J^{2x}_{m-r} can be analytically evaluated [*Abramowitz and Stegun*, 1972; *Costa and Basu*, 2002]. Representations for I^{1y}_{n-s}, J^{2y}_{n-s}, and β_y can be obtained from equations (B11)–(B13) by trivial changes of indices. Designing individual changes of indices for each of the four double summations in equation (B10) such that the samples $u_{r,s}$, $u_{r+1,s}$, $u_{r,s+1}$, and $u_{r+1,s+1}$ become $u_{m-R,n-S}$ (that is, $r, s \to m\text{-}R,n\text{-}S$; $r+1, s \to m\text{-}R,n\text{-}S$; $r,s+1 \to m\text{-}R,n\text{-}S$; and $r+1,\ s+1 \to m\text{-}R,n\text{-}S$; respectively), and multiplying the result by the phase term in the right-hand side of equation (B7), one gets

$$u_{m,n}(z-\delta z) = e^{i\frac{k(\eta^2-1)}{2d_z}\delta z}\sum_{R=-\infty}^{+\infty}\sum_{S=-\infty}^{+\infty} C^x_R\ C^y_S\ u_{m-R,n-S}(z) \tag{B14}$$

where

$$C^x_R = \frac{1}{\sqrt{2i}}\left\{\left[(R+1)I^{1x}_{R+1} - J^{2x}_{R+1}\right] - \left[(R-1)I^{1x}_{R} - J^{2x}_{R}\right]\right\} \tag{B15}$$

and C^y_S is also obtained from the above equation by trivial changes of indices. Equation (B14) is the discrete version of equation (B7). It is easily concluded by inspection that the coefficients C^x_R and C^y_S can be calculated as prescribed by equations (21)–(25) in the work of *Costa and Basu* [2002]. The following discussions of the above reference are also immediate and directly applicable to the present work: (1) those in paragraphs [8]–[10] related to errors in the solution of the parabolic equation by the split-step method and to the need of keeping the step size δz sufficiently small; (2) those in paragraphs [11], [12] and [18], showing some difficulties in the straightforward numerical evaluation of the convolution integral (B7), in comparison with the asymptotically decrease of the coefficients C^x_R and

C_S^v; (3) programming notes at the ends of paragraphs [13] and [17]. Therefore, they will not be repeated here.

[40] The final expression for the discrete version of the phase-screen theory is determined from a straightforward analogy between equations (B7) and (B14). Similarly, the infinite double summation in equation (B14) should tend to one in absolute value, in the special case $u_{m-R,\,n-S} = 1$. This result should be considered in the truncation of the summation limits.

[41] To proceed with the propagation calculations based on equation (B14), the refractive index of the irregularity layer should be specified. It is known that

$$\eta^2(\vec{r}) - 1 = -\frac{r_e \lambda^2}{\pi}[N_o(z) + \delta N(\vec{r})] \qquad \text{(B16)}$$

where $N_o(z)$ is the background electron density at height z and δN represents random electron density fluctuations. It will be assumed that the background electron density profile is deterministic and that it remains constant during the extremely short time interval needed to characterize scintillation. Therefore, it only contributes a fixed phase to the received signal, which can be ignored in the present application. Substituting the random part of expression (B16) into equation (B14) and expressing the coefficients C_R^α and C_S^v as indicated by *Costa and Basu* [2002], the propagation algorithm described in section 3 is obtained.

[42] **Acknowledgments.** The authors thank Acácio C. Neto (INPE, São Luís, MA, Brazil) and his staff for the radar operation and maintenance, Lázaro P. de Camargo (INPE, São José dos Campos, SP, Brazil) for processing of the RTI data, and Esfhan A. Kherani (INPE, São José dos Campos, SP, Brazil) and Fabiano S. Rodrigues (ASTRA, San Antonio, TX, USA) for many enlightening discussions. The authors also thank Donald Hunton (AFRL/RVBXT) and the reviewers for their detailed and insightful comments and constructive suggestions. Their valuable contributions helped the authors to produce an improved paper. Work at CETUC/PUC-Rio has been sponsored by the Air Force Office of Scientific Research (AFOSR) under award FA9550-07-1-0586.

References

Abramowitz, M., and I. A. Stegun (1972), *Handbook of Mathematical Functions*, Dover, New York.

Arruda, D. C. S., J. H. A. Sobral, M. A. Abdu, V. M. Castilho, H. Takahashi, A. F. Medeiros, and R. A. Buriti (2006), Theoretical and experimental zonal drift velocities of the ionospheric plasma bubbles over the Brazilian region, *Adv. Space Res.*, *38*, 2610–2614, doi:10.1016/j.asr.2006.05.015.

Basu, S., S. Basu, J. Aarons, J. P. McClure, and M. D. Cousins (1978), On the coexistence of kilometer- and meter-scale irregularities in the nighttime equatorial *F* region, *J. Geophys. Res.*, *83*, 4219–4226, doi:10.1029/JA083iA09p04219.

Basu, S., S. Basu, J. P. McClure, W. B. Hanson, and H. E. Whitney (1983), High resolution topside in situ data of electron densities and VHF/GHz scintillations in the equatorial region, *J. Geophys. Res.*, *88*, 403–415, doi:10.1029/JA088iA01p00403.

Basu, S., E. MacKenzie, and S. Basu (1988), Ionospheric constraints on VHF/UHF communications links during solar maximum and minimum periods, *Radio Sci.*, *23*, 363–378, doi:10.1029/RS023i003p00363.

Basu, S., K. M. Groves, Su. Basu, and P. J. Sultan (2002), Specification and forecasting of scintillations in communication/navigation links: Current status and future plans, *J. Atmos. Sol. Terr. Phys.*, *64*, 1745–1754, doi:10.1016/S1364-6826(02)00124-4.

Beach, T. L., T. R. Pedersen, M. J. Starks, and S. Y. Su (2004), Estimating the amplitude scintillation index from sparsely sampled phase screen data, *Radio Sci.*, *39*, RS5001, doi:10.1029/2002RS002792.

Caton, R. G., W. J. McNeil, K. M. Groves, and S. Basu (2004), GPS proxy model for real-time UHF satellite communications scintillation maps from the Scintillation Network Decision Aid (SCINDA), *Radio Sci.*, *39*, RS1S22, doi:10.1029/2002RS002821.

Costa, E., and S. Basu (2002), A radio wave scattering algorithm and irregularity model for scintillation predictions, *Radio Sci.*, *37*(3), 1046, doi:10.1029/2001RS002498.

Costa, E., and M. C. Kelley (1978), On the role of steepened structures and drift waves in equatorial spread *F*, *J. Geophys. Res.*, *83*, 4359–4364, doi:10.1029/JA083iA09p04359.

de La Beaujardière, O., et al. (2004), C/NOFS: A mission to forecast scintillation, *J. Atmos. Sol. Terr. Phys.*, *66*, 1573–1591, doi:10.1016/j.jastp.2004.07.030.

de Paula, E. R., and D. L. Hysell (2004), The São Luís 30 MHz coherent scatter ionospheric radar: System description and initial results, *Radio Sci.*, *39*, RS1014, doi:10.1029/2003RS002914.

de Paula, E. R., F. S. Rodrigues, K. N. Iyer, I. J. Kantor, M. A. Abdu, P. M. Kintner, B. M. Ledvina, and H. Kil (2003), Equatorial anomaly effects on GPS scintillations in Brazil, *Adv. Space Res.*, *31*, 749–754, doi:10.1016/S0273-1177(03)00048-6.

Dyson, P. L., J. P. McClure, and W. B. Hanson (1974), In situ measurements of the spectral characteristics of *F* region ionospheric irregularities, *J. Geophys. Res.*, *79*, 1497–1502, doi:10.1029/JA079i010p01497.

Fougere, P. F. (1985), On the accuracy of spectrum analysis of red noise processes using maximum entropy and periodogram methods: Simulation studies and application to geophysical data, *J. Geophys. Res.*, *90*, 4355–4366, doi:10.1029/JA090iA05p04355.

Goodman, J. W. (1968), *Introduction to Fourier Optics*, McGraw-Hill, New York.

Groves, K. M., et al. (1997), Equatorial scintillation and systems support, *Radio Sci.*, *32*, 2047–2064, doi:10.1029/97RS00836.

Haerendel, G. (1973), Theory of equatorial spread *F*, report, Max-Planck Inst. for Extraterr. Phys., Garching, Germany.

Heelis, R. A., R. Stoneback, G. D. Earle, R. A. Haaser, and M. A. Abdu (2010), Medium-scale equatorial plasma irregularities observed by Coupled Ion-Neutral Dynamics Investigation sensors aboard the Communication Navigation Outage Forecast System in a prolonged solar minimum, *J. Geophys. Res.*, *115*, A10321, doi:10.1029/2010JA015596.

Hysell, D. L. (2000), An overview and synthesis of plasma irregularities in equatorial spread *F*, *J. Atmos. Sol. Terr. Phys.*, *62*, 1037–1056, doi:10.1016/S1364-6826(00)00095-X.

Hysell, D. L., and J. Burcham (1998), JULIA radar studies of equatorial spread *F*, *J. Geophys. Res.*, *103*, 155–167, doi:10.1029/98JA02655.

Hysell, D. L., M. C. Kelley, W. E. Swartz, R. F. Pfaff, and C. M. Swenson (1994a), steepened structures in equatorial spread *F*: 1. New observations, *J. Geophys. Res.*, *99*, 8827–8840, doi:10.1029/93JA02961.

Hysell, D. L., M. C. Kelley, W. E. Swartz, and D. T. Farley (1994b), VHF radar and rocket observations of equatorial spread *F* on Kwajalein, *J. Geophys. Res.*, *99*, 15,065–15,085, doi:10.1029/94JA00476.

Ishimaru, A. (1997), *Wave Propagation and Scattering in Random Media*, IEEE Press-Oxford Univ. Press Classic Reissue, New York.

Kelley, M. C. (1989), *The Earth's Ionosphere: Plasma Physics and Electrodynamics*, *Int. Geophys. Ser.*, vol. 43, Academic, San Diego, Calif.

Kelley, M. C., and R. Livingston (2003), Barium cloud striations revisited, *J. Geophys. Res.*, *108*(A1), 1044, doi:10.1029/2002JA009412.

Kelley, M. C., G. Haerendel, H. Kappler, A. Valenzuela, B. B. Balsley, D. A. Carter, W. L. Ecklund, C. W. Carlson, B. Hausler, and R. Torbet (1976), Evidence for a Rayleigh-Taylor type instability and upwelling of depleted density regions during equatorial spread *F*, *Geophys. Res. Lett.*, *3*, 448–450, doi:10.1029/GL003i008p00448.

Kelley, M. C., et al. (1986), The Condor equatorial spread *F* campaign: Overview and results of the large-scale measurements, *J. Geophys. Res.*, *91*, 5487–5503, doi:10.1029/JA091iA05p05487.

Knepp, D. (1983), Multiple phase-screen calculation of the temporal behavior of stochastic waves, *Proc. IEEE*, *71*, 722–737, doi:10.1109/PROC.1983.12660.

Kuttler, J. R., and G. D. Dockery (1991), Theoretical description of the parabolic approximation/Fourier split-step method of representing electromagnetic propagation in the troposphere, *Radio Sci.*, *26*, 381–393, doi:10.1029/91RS00109.

LaBelle, J., M. C. Kelley, and C. E. Seyler (1986), An analysis of the role of drift waves in equatorial spread *F*, *J. Geophys. Res.*, *91*, 5513–5525, doi:10.1029/JA091iA05p05513.

LaBelle, J., J. M. Jahn, R. F. Pfaff, W. E. Swartz, J. H. A. Sobral, M. A. Abdu, P. Muralikrishna, and E. R. de Paula (1997), The Brazil/Guará equatorial spread *F* campaign: Results of the large scale measurements, *Geophys. Res. Lett.*, *24*, 1691–1694, doi:10.1029/97GL00818.

Muella, M. T. A. H., E. A. Kherani, E. R. de Paula, A. P. Cerruti, P. M. Kintner, I. J. Kantor, C. N. Mitchell, I. S. Batista, and M. A. Abdu (2010), Scintillation-producing Fresnel-scale irregularities associated with the regions of steepest TEC gradients adjacent to the equatorial ionization anomaly, *J. Geophys. Res.*, *115*, A03301, doi:10.1029/2009JA014788.

Muralikrishna, P., L. P. Vieira, M. A. Abdu, and E. R. de Paula (2003), On the deviations of measured electron density profiles from IRI predictions for low latitudes, *Adv. Space Res.*, *31*, 563–568, doi:10.1016/S0273-1177(03)00035-8.

Retterer, J. M. (2010), Forecasting low-latitude radio scintillation with 3-D ionospheric plume models: 2. Scintillation calculation, *J. Geophys. Res.*, *115*, A03307, doi:10.1029/2008JA013840.

Rino, C. L., and J. Owen (1984), Numerical simulation of intensity scintillation using the power law phase screen model, *Radio Sci.*, *19*, 891–908, doi:10.1029/RS019i003p00891.

Rino, C. L., R. T. Tsunoda, J. Petriceks, R. C. Livingston, M. C. Kelley, and K. D. Baker (1981), Simultaneous rocket-borne beacon and in situ measurements of equatorial spread *F*–intermediate wavelength results, *J. Geophys. Res.*, *86*, 2411–2420, doi:10.1029/JA086iA04p02411.

Rodrigues, F. S., E. R. de Paula, M. A. Abdu, A. C. Jardim, K. N. Iyer, P. M. Kintner, and D. L. Hysell (2004), Equatorial spread *F* irregularity characteristics over São Luís, Brazil, using VHF radar and GPS scintillation techniques, *Radio Sci.*, *39*, RS1S31, doi:10.1029/2002RS002826.

Rodrigues, F. S., D. L. Hysell, and E. R. de Paula (2008), Coherent backscatter radar imaging in Brazil: Large-scale waves in the bottomside *F* region at the onset of equatorial spread *F*, *Ann. Geophys.*, *26*, 3355–3364, doi:10.5194/angeo-26-3355-2008.

Santana, D. C., J. H. A. Sobral, H. Takahashi, and M. J. Taylor (2001), Optical studies of the ionospheric irregularities over the Brazilian region by nocturnal images of the OI 630 nm emission, *Adv. Space Res.*, *27*(6–7), 1207–1212, doi:10.1016/S0273-1177(01)00199-5.

Singh, M., and E. P. Szuszczewicz (1984), Composite equatorial spread *F* wave number spectra from medium to short wavelengths, *J. Geophys. Res.*, *89*, 2313–2323, doi:10.1029/JA089iA04p02313.

Tsunoda, R., R. Livingston, J. McClure, and W. Hanson (1982), Equatorial plasma bubbles: Vertically elongated wedges from the bottomside *F* layer, *J. Geophys. Res.*, *87*, 9171–9180, doi:10.1029/JA087iA11p09171.

Walker, A., R. Greenwald, and K. Baker (1987), Determination of the fluctuation level of ionospheric irregularities from radar backscatter measurements, *Radio Sci.*, *22*(5), 689–705, doi:10.1029/RS022i005p00689.

Wernik, A. W., C. H. Liu, and K. C. Yeh (1980), Model computations of radio wave scintillation caused by equatorial ionospheric plasma bubbles, *Radio Sci.*, *15*, 559–572, doi:10.1029/RS015i003p00559.

Woodman, R. F. (2009), Spread *F*—An old equatorial aeronomy problem finally resolved?, *Ann. Geophys.*, *27*, 1915–1934, doi:10.5194/angeo-27-1915-2009.

Woodman, R. F., and S. Basu (1978), Comparison between in situ spectral measurements of *F* region irregularities and backscatter observations at 3 m wavelength, *Geophys. Res. Lett.*, *5*, 869–872, doi:10.1029/GL005i010p00869.

Woodman, R. F., and C. LaHoz (1976), Radar observations of *F* region equatorial irregularities, *J. Geophys. Res.*, *81*, 5447–5466, doi:10.1029/JA081i031p05447.

Yeh, K. C., and C. H. Liu (1982), Radio wave scintillation in the ionosphere, *Proc. IEEE*, *70*, 324–360, doi:10.1109/PROC.1982.12313.

E. Costa, Centro de Estudos em Telecomunicações, Pontifícia Universidade Católica do Rio de Janeiro, Rua Marquês de São Vicente 225, 22451-900 Rio de Janeiro, RJ, Brazil. (epoc@cetuc.puc-rio.br)

E. V. Dao and M. C. Kelley, School of Electrical and Computer Engineering, Cornell University, Frank H. T. Rhodes Hall, Room 320, Ithaca, NY 14853, USA. (mikek@ece.cornell.edu)

E. R. de Paula and L. F. C. Rezende, Divisão de Aeronomia, Instituto Nacional de Pesquisas Espaciais, Av. dos Astronautas 1758, 12201-970 São José dos Campos, SP, Brazil. (eurico@dae.inpe.br; luizfelipe@dae.inpe.br)

K. M. Groves and P. A. Roddy, Space Vehicles Directorate, Air Force Research Laboratory, 29 Randolph Rd., Hanscom AFB, MA 01731, USA. (keith.groves@hanscom.af.mil; patrick.roddy@hanscom.af.mil)